CrossMark

M-shaped asymmetric nonlinear oscillator for broadband vibration energy harvesting: Harmonic balance analysis and experimental validation

S. Leadenham *, A. Erturk

G.W. Woodruff School of Mechanical Engineering, Georgia Institute of Technology, Atlanta, GA 30332, USA

ARTICLE INFO

ABSTRACT

Over the past few years, nonlinear oscillators have been given growing attention due to their ability to enhance the performance of energy harvesting devices by increasing the frequency bandwidth. Duffing oscillators are a type of nonlinear oscillator characterized by a symmetric hardening or softening cubic restoring force. In order to realize the cubic nonlinearity in a cantilever at reasonable excitation levels, often an external magnetic field or mechanical load is imposed, since the inherent geometric nonlinearity would otherwise require impractically high excitation levels to be pronounced. As an alternative to magnetoelastic structures and other complex forms of symmetric Duffing oscillators, an M-shaped nonlinear bent beam with clamped end conditions is presented and investigated for bandwidth enhancement under base excitation. The proposed M-shaped oscillator made of spring steel is very easy to fabricate as it does not require extra discrete components to assemble, and furthermore, its asymmetric nonlinear behavior can be pronounced yielding broadband behavior under low excitation levels. For a prototype configuration, linear and nonlinear system parameters extracted from experiments are used to develop a lumped-parameter mathematical model. Quadratic damping is included in the model to account for nonlinear dissipative effects. A multi-term harmonic balance solution is obtained to study the effects of higher harmonics and a constant term. A single-term closed-form frequency response equation is also extracted and compared with the multi-term harmonic balance solution. It is observed that the single-term solution overestimates the frequency of upper saddle-node bifurcation point and underestimates the response magnitude in the large response branch. Multi-term solutions can be as accurate as time-domain solutions, with the advantage of significantly reduced computation time. Overall, substantial bandwidth enhancement with increasing base excitation is validated experimentally, analytically, and numerically. As compared to the 3 dB bandwidth of the corresponding linear system with the same linear damping ratio, the M-shaped oscillator offers 3200, 5600, and 8900 percent bandwidth enhancement at the root-mean-square base excitation levels of $0.03g$, $0.05g$, and $0.07g$, respectively. The M-shaped configuration can easily be exploited in piezoelectric and electromagnetic energy harvesting as well as their hybrid combinations due to the existence of both large strain and kinetic energy regions. A demonstrative case study is given for electromagnetic energy harvesting, revealing the importance of higher harmonics and the need for multi-term harmonic balance analysis for predicting the electrical power output accurately.

© 2014 Elsevier Ltd. All rights reserved.

---

* Corresponding author.
  E-mail address: sleadenham@gatech.edu (S. Leadenham).

1. Introduction

Research on energy harvesting methods and technologies has received growing attention over the last decade [1,2]. The motivation in vibration-based energy harvesting is to power small electronic devices (such as wireless sensor networks used in passive and active monitoring applications) by using the vibrational energy available in their environments. Researchers have reported their work on modeling and applications of vibration-based energy harvesting using electromagnetic [3–5], electrostatic [6–8], piezoelectric [9–11] and magnetostrictive [12,13] transduction mechanisms, as well as electronic and ionic electroactive polymers [14,15]. In particular, due to the high power density and ease of application of piezoelectric materials, piezoelectric energy harvesting has received the most attention [1,16–19].

The most commonly used piezoelectric energy harvester configuration is a cantilever with piezoceramic layers located on a vibrating host structure for electrical power generation from bending vibrations under resonance excitation. Such a design that operates effectively only at its linear resonance frequency is called a resonant energy harvester. Theoretical and experimental aspects of the linear cantilever design have been investigated extensively in the literature [9,10,20,21]. A major limitation of the commonly employed resonant energy harvester configuration is that the effective power generation performance of the device is limited to resonance excitation. If the excitation frequency deviates slightly from the fundamental resonance frequency of the energy harvester (due to changing excitation or environmental conditions or manufacturing imperfections of the harvester device), the electrical power output is reduced by orders of magnitude. In order to overcome the bandwidth issue of the conventional cantilever configuration, researchers [22] have recently considered exploiting nonlinear dynamic phenomena [23,24].

Implementations of the hardening stiffness of the monostable Duffing oscillator for increasing the frequency bandwidth were discussed by Burrow et al. [25] and Mann and Sims [26] for electromagnetic energy harvesting. Use of the hardening stiffness in the monostable form of the Duffing oscillator was also discussed by Ramlan et al. [27] along with snap-through behavior in a bistable mass-spring-damper mechanism. Random excitation of monostable Duffing oscillators was theoretically investigated by Daqaq [28] and Green et al. [29]. Bidirectional increase of the frequency bandwidth was studied by combining the softening and the hardening stiffness effects in the device proposed by Stanton et al. [30]. The bistable form of the Duffing oscillator was discussed by Cottone et al. [31] and Gammaitoni et al. [32] for noise excitation. Additionally, the concept of stochastic resonance in bistable systems was pointed out by McInnes et al. [33] for use in energy harvesting. Stanton et al. [34] theoretically investigated the bifurcations of a bistable configuration similar to the one tested by Cottone et al. [31] and also presented harmonic balance analysis using a single harmonic [35]. Another important aspect of the bistable Duffing oscillator has been pointed out by Erturk et al. [36] for piezoelectric energy harvesting using a magnetoelastic structure [37]. Large-amplitude interwell oscillations [24] on high-energy orbits of the bistable configuration have been shown to increase the power output by an order of magnitude at several frequencies [38]. Other than magnetoelastic interactions [30,34–36,38,39], purely elastic buckling was also considered for bandwidth and performance enhancement in energy harvesting [40–42]. A bistable electromagnetic energy harvester was theoretically and experimentally explored by Mann and Owens [43]. In electrostatic energy harvesting, MEMS bistable spring arrangements for bandwidth enhancement were presented by Nguyen et al. [44]. Random excitation of bistable energy harvesters have been studied by using analytical [45–47], numerical [48–50], and experimental [50] methods. Recent efforts also include the investigation of nonlinear damping for extending the dynamic range in energy harvesters [51]. An extensive review on the use of nonlinearities in vibration energy harvesting can be found in a recent article by Daqaq et al. [22]. Other review articles on broadband energy harvesting methods are due to Tang et al. [52], Pellegrini et al. [53], Twiefel and Westermann [54], and Harne and Wang [55].

Most of the existing literature of energy harvesting at meso-scale exploits magnetoelastic interactions with discrete components (e.g. magnets) and buckled structures to create nonlinearities [30,34–36,38,40–43]. Furthermore, energy harvesters employing purely elastic [40–42] or magnetoelastic [30,34–36,38] buckling often require significantly large excitation levels (on the order of 1*g*) to fully exploit large-amplitude nonlinear dynamic phenomena. The present work focuses on the meso-scale implementation, experimentally validated modeling, and analysis of a nonlinear spring architecture formerly used in MEMS-scale [56,57] electrostatic energy harvesting.

Fig. 1 summarizes the physical motivation for the M-shaped oscillator explored in this work and its advantages over the standard clamped–clamped monostable and bistable configurations. A clamped–clamped beam with no compressive preload, as shown in Fig. 1a, can exhibit hardening nonlinearity to increase response bandwidth as well as protect against dangerously large strains in attached piezoelectric laminates. However, since hardening is due to the relatively large axial stiffness opposing extensional deformation, maximum deflections will be small, severely limiting power generation
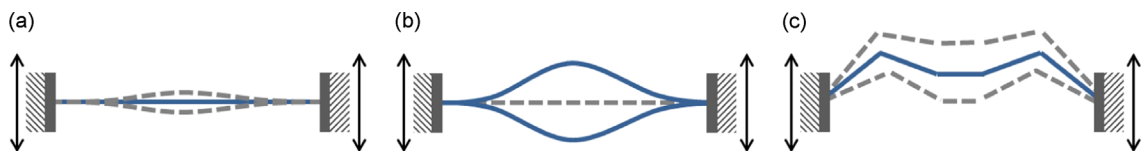

Fig. 1. Clamped–clamped beams under base excitation: (a) monostable configuration with no compressive preload (exhibits limited stretching capability); (b) bistable configuration due to compressive axial preloading (requires large excitation for interwell oscillations); and (3) pre-bent nonlinear M-shaped monostable configuration (exhibits large stretching capability) studied in this work. Solid blue lines indicate the static equilibrium configurations. (For interpretation of the references to color in this figure legend, the reader is referred to the web version of this article.)

capabilities. As depicted in Fig. 1b, introducing a compressive axial preload to induce buckling yields a structure that can snap between two large deflection configurations (as long as the potential wells [58] are overcome in response to dynamic excitation), greatly increasing power output while still maintaining upper limits on piezoelectric laminate deformation. Dynamic snap-through behavior [40–42] typically requires large excitation levels, limiting bistable energy harvesters to high excitation applications. A pre-bent monostable beam structure, the M-shaped configuration shown in Fig. 1c, can exhibit both limited maximum deflections to protect piezoelectric laminates and advantageous nonlinear dynamic behavior at low excitation levels due to large stretching capabilities. In the present work, the nonlinear dynamic behavior of the system is explored through experiments and multi-term harmonic balance modeling, in addition to presenting a simple platform for broadband piezoelectric and electromagnetic energy harvesting as well as their hybrid configurations.

In the following, first the M-shaped bent beam configuration with clamped end conditions is described for broadband vibration energy harvesting under base excitation. The focus is placed on the experimental system and identification of the linear and nonlinear system parameters for modeling and nonlinear analysis. The force−displacement relationship of the M-shaped beam with a central lumped mass attachment is experimentally obtained and asymmetric nonlinear behavior is verified. Linear and nonlinear system parameters extracted from experiments are used to develop a lumped-parameter mathematical model. A multi-term harmonic balance solution is obtained to study the effects of higher harmonics and a constant steady-state term resulting from asymmetry. A single-term closed-form frequency response equation is also extracted and compared with the multi-term harmonic balance solution. Finally, a case study is given for electromagnetic energy harvesting to further demonstrate the importance of higher terms in the harmonic balance analysis.

2. M-shaped nonlinear oscillator and energy harvester configurations

Top and isometric views of the M-shaped oscillator configuration along with its clamp and shaker mount are shown in Fig. 2. Although this configuration can be fabricated at different geometric scales, the M-shaped oscillator analyzed in this work consists of a beam made from 25.4 mm wide by 0.254 mm thick AISI 1075 spring steel. The steel is cut and bent using common sheet metal tools. The bend angles used are small enough to allow near zero radius bends without first heating the metal. The lumped mass attachment consists of eight $12.7 \times 12.7 \times 3.18$ mm^3 permanent magnets, half on each side of the spring. Magnets are chosen due to their ease of attachment to the steel spring, rather than to subject the system to any magnetic force effects, therefore the lumped mass does not have to be made of magnets, and likewise the M-shaped structure does not have to be ferromagnetic. The total lumped mass attachment is 30.4 g. Both ends of the oscillator are clamped. The clamp and shaker mount are made from 6061 aluminum.

While the present work is focused mainly on the nonlinear oscillator structure, electrical power generation can be achieved by adding proper electromechanical coupling interface elements to the elastic oscillator. Fig. 3a shows the M-shaped oscillator with four piezoelectric patches bonded near the clamps (resulting in two bimorphs). Dynamic bending of the spring causes tensile and compressive strains on the piezoelectric layers, yielding an alternating voltage via the direct piezoelectric effect, which is then connected to an electrical load for AC power generation or rectified and conditioned in an energy harvesting circuit to obtain a stable DC signal for charging a storage component [59–62]. If a permanent magnet is used as the proof mass, power may be generated by attaching a coil to the base of the oscillator, as shown in Fig. 3b. The motion of the permanent magnet relative to the coil creates a changing magnetic field inside the coil, which according to Faraday's law produces a current in the coil. The AC electrical output is then connected to the load or a proper electromagnetic energy harvesting circuit. Both of these electromechanical coupling methods can be employed simultaneously. The resulting hybrid piezoelectric−electromagnetic energy harvester is shown in Fig. 3c. In the present effort, focus is predominantly placed on the purely mechanical nonlinear dynamics of the M-shaped structure.
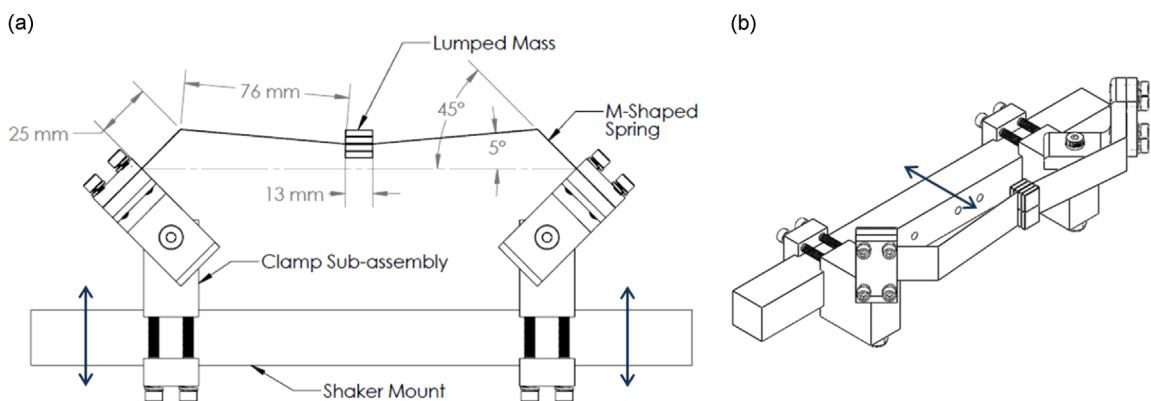

Fig. 2. (a) Top and (b) isometric model views of M-shaped oscillator with its fixture. Vibration input is provided from the shaker mount (arrows indicating the direction of mechanical base excitation).
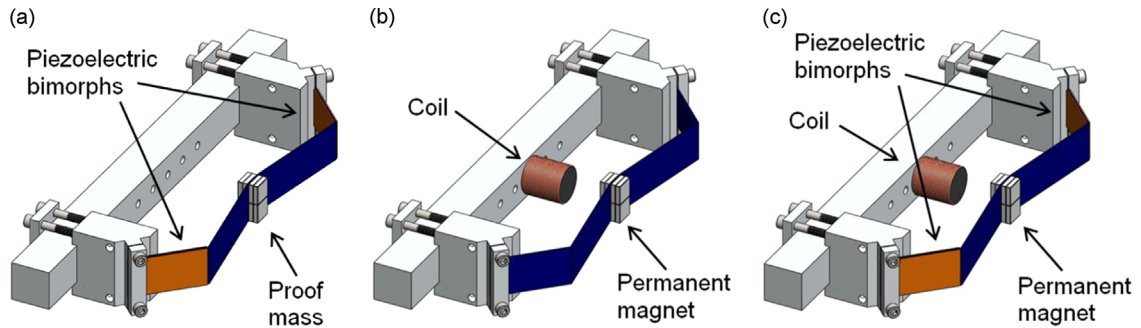
Fig. 3. M-shaped piezoelectric and/or electromagnetic energy harvester configurations employing (a) piezoelectric patches attached to high strain energy regions, (b) a coil-magnet arrangement attached to high kinetic energy region, and (c) combination of the previous two to form a hybrid design. Terminals of the piezoelectric patches and/or coil are connected to electrical loads or a more complex energy harvesting circuit.
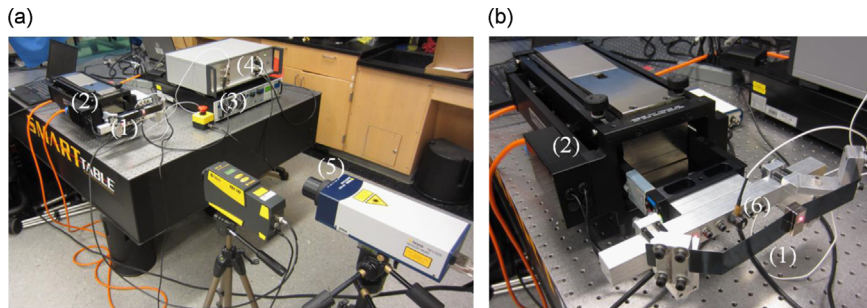

Fig. 4. (a) Overview and (b) detail pictures of experimental setup: (1) M-shaped oscillator; (2) long-stroke shaker; (3) amplifier; (4) controller; (5) laser vibrometers; and (6) accelerometer. The M-shaped oscillator is attached to the armature of the shaker through its fixture for horizontal base excitation.

3. Experimental system, mathematical model, and parameter identification

This section introduces the experimental system used for testing and analyzing the M-shaped nonlinear oscillator prototype. The stiffness, mass, and damping properties of the M-shaped oscillator are identified and tabulated prior to nonlinear modeling and analyses in the next sections.

3.1. Experimental setup

Experiments are conducted using an APS-113 seismic shaker driven by an APS-125 amplifier and controlled by a SPEKTRA VCS-201 controller. These devices allow for the sample to be subjected to harmonic base acceleration at specified amplitudes and frequencies. Tests consist of up and down frequency sweeps at a constant kinematic variable (in this case base acceleration amplitude) necessary for frequency response analysis of the nonlinear system. Base acceleration measured by a Kistler model 8636C50 ICP accelerometer is used for feedback to the VCS-201 controller. A Polytec PDV-100 Portable Digital Vibrometer is used to measure the base velocity. The velocity and displacement of the lumped mass (i.e. center of the M-shaped oscillator) are measured using a Polytec OFV-505 sensor head and OFV-5000 controller with a displacement decoder. Data is acquired using a National Instruments NI USB-4431 unit. Overview and detail views of the experimental setup are shown in Fig. 4.

3.2. Mathematical model

The M-shaped oscillator is modeled as a single-degree-of-freedom system with linear viscous and quadratic damping terms along with a nonlinear elastic restoring force undergoing base excitation (Fig. 5). The equation of motion of such a system is

$$m\ddot{z}+2\zeta m\omega_n\dot{z}(1+\gamma|\dot{z}|)+f(z)=-m'\ddot{y} \tag{1}$$

where m is the equivalent mass of the oscillator, m' is the effective mass that causes the forcing term due to base excitation ($m'=m$ if the spring mass is negligible as compared to the lumped mass attachment), ζ is the linear viscous damping ratio, γ is a constant that accounts for the quadratic damping, ω_n is the linear natural frequency, $f(z)$ is the nonlinear elastic restoring force, $y(t)$ is the base displacement measured in an inertial frame, $z(t)$ is the displacement of the oscillator relative
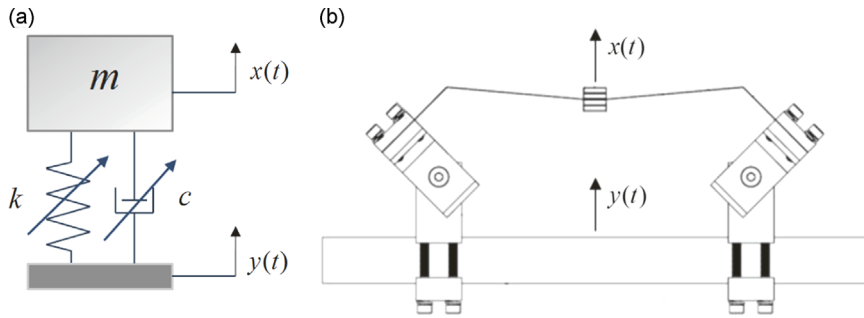
Fig. 5. (a) Lumped-parameter model and (b) device schematics of the M-shaped nonlinear oscillator under base excitation (stiffness and damping components are nonlinear).
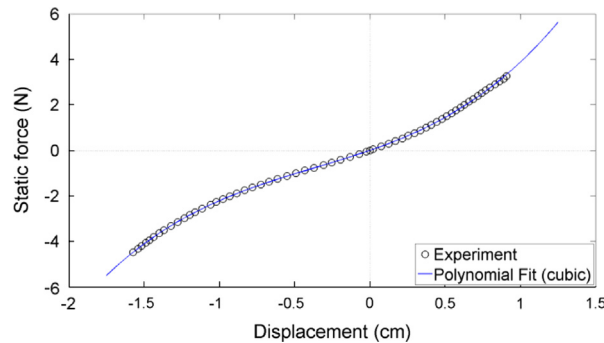

Fig. 6. Experimental static force–displacement relationship and third-order polynomial curve fit.

to the moving base, and an overdot represents differentiation with respect to time. Note that the displacement of the mass relative to the fixed reference frame is denoted by $x(t)$ in Fig. 5, therefore the displacement relative to the base is $z(t) = x(t) - y(t)$.

3.3. Parameter identification

In order to investigate the nonlinear system dynamics theoretically, it is necessary to identify the relevant parameters of the M-shaped oscillator. First the relationship between deflection and restoring force, $f(z)$, is extracted. To this end, the oscillator is bolted to the rigid optical table vertically (to set $y=0$ so that $x=z$). With the lumped mass attachment removed (to avoid any sag due to gravity), weights are suspended from the center of the spring. Deflection is measured using the OFV-5000 displacement decoder of the laser vibrometer. The sample is turned over and the process repeated. It is assumed that the weight of the spring itself is negligible compared to the suspended weights. Reasonably, it is also assumed the removal of the mass attachments does not change the stiffness characteristics of the spring. As shown in Fig. 6, a third-order polynomial of the following form is fit to the measured force–displacement data:

$$f(z) = k_1 z + k_2 z^2 + k_3 z^3 \qquad (2)$$

where $k_1 = 229.61$ N/m, $k_2 = 8289.4$ N/m^2, and $k_3 = -750{,}840$ N/m^3 are constant coefficients on the first, second, and third-order terms, respectively (in particular, $k_1 = m\omega_n^2$). Any constant term (coefficient of zeroth-order term) of the polynomial fit is set to be zero, as the force–displacement relationship should pass through the origin. The linear coefficient can be interpreted as the linear spring stiffness, and the cubic and quadratic coefficients as the symmetric and asymmetric nonlinear stiffness terms, respectively. Note that the inflection point of the curve occurs in Fig. 6 at a deflection of approximately 5 mm. The amount of asymmetry depends on the overall structural design and geometric parameters. While the much smaller asymmetry leads to an expectation of more classical Duffing oscillator behavior, the asymmetry is present, and further investigation on the relationship between the multiple geometric parameters of the spring design and its force–displacement characteristics is of interest for future research.

In order to identify the linear damping and linear natural frequency of the system, the M-shaped oscillator (with mass attachments) is clamped horizontally to the table (to eliminate any displacements and sag due to gravity in the presence of the proof mass) and given a small initial excitation. The measured displacement time series for the linear free vibration test is shown in Fig. 7. It is known from the elementary theory of vibrations [63,64] that the natural response of a linear
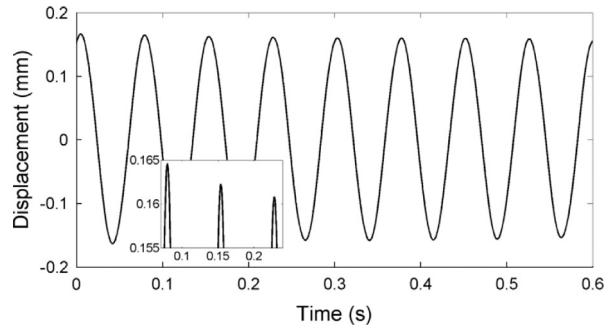
Fig. 7. Time series of free vibration for linear parameter identification.

Table 1
Identified linear and nonlinear model parameters.

k_1	229.61 N/m
k_2	8289.4 N/m^2
k_3	750840 N/m^3
ω_n	84.3 rad/s
ζ	0.0011
γ	1 s/m
m	0.0323 kg

underdamped system decays in an exponential envelope as

$$x(t) = Xe^{-\xi\omega_n t} \cos(\omega_d t - \phi) \tag{3}$$

where $\omega_d = \omega_n\sqrt{1-\zeta^2}$ is the damped natural frequency. Fitting an exponential curve to the peaks of the time series yields $\zeta\omega_n$. The damped natural frequency is found from the period of oscillation. Damping for this system is extremely light, so the approximation $\omega_n \cong \omega_d$ is used safely. Therefore the values of $\omega_n = 84.3$ rad/s and $\zeta = 0.0011$ are obtained for the natural frequency and damping ratio, respectively.

The equivalent mass is obtained from the linear stiffness component and natural frequency as $m = k_1/\omega_n^2 = 0.0323$ kg. This identified equivalent mass of 32.3 g is consistent with the value of the attached mass of 30.4 g. The proof mass attachment indeed makes up the majority of the equivalent mass as intended, and the contribution from the effective spring mass is minor.

Finally, the quadratic damping term (γ) in Eq. (1) is found to be necessary, as without it, the model tended to overestimate the amplitude and frequency of the upper saddle-node bifurcation point at which the jump phenomenon [24] takes place in the up sweep in the frequency response curves. The physical justification of quadratic (or velocity-squared) damping is nonlinear fluid damping (see, for instance, Bandstra [65], among others). It is indeed plausible that nonlinear air damping [65] would be significant, as velocities in excess of 1 m/s were observed in the experiments (see Eq. (1) and note that the identified value of nonlinear damping term is $\gamma = 1$ s/m, i.e. the linear and nonlinear dissipation components are on the same order of magnitude). The value of γ is estimated from the comparison of experimental and simulated response curves discussed in Section 5.1. The identified linear and nonlinear model parameters are summarized in Table 1.

4. Nonlinear analysis using the method of harmonic balance

The second-order nonlinear equation of motion, Eq. (1), can be expressed in the form of two nonlinear first-order equations for time-domain numerical simulations (e.g. by using ode45 in MATLAB). However, numerical simulation in time domain to generate frequency response curves is undesirable, since the process can be computationally lengthy, numerical errors may build up over the course of the simulation, and little insight into the underlying mathematics of the problem is gleaned. A number of approximate solution and perturbation methods exist for the analysis of nonlinear ordinary differential equations, such as the Poincaré–Lindstedt method, the method of multiple scales, the Krylov–Bogoliubov averaging method, and the method of harmonic balance [66]. The system studied here exhibits a high degree of nonlinearity and therefore it is required to explore multi-harmonic solutions for enhanced accuracy. Harmonic balance is the analysis method that most easily accommodates multi-term approximate solutions. In the following, first the multi-harmonic solution is given by accounting for higher harmonics and a DC (constant) component, and then the single-harmonic solution with a closed-form frequency response equation is presented.

4.1. Multi-harmonic solution

The base excitation term is assumed to be harmonic of the form

$$\ddot{y}(t) = A \cos(\Omega t) \tag{4}$$

where A is the acceleration amplitude and Ω is the driving frequency. A Fourier series solution with the same period as the forcing is assumed for the vibration response ($z(t) = x(t) - y(t)$) relative to the moving base (see Fig. 5). The displacement, velocity, and acceleration of the mass relative to the moving base are then

$$z(t) = a_0 + \sum_{n=1}^{\infty} [a_n \cos(n\Omega t) + b_n \sin(n\Omega t)] = a_0 + \sum_{n=1}^{\infty} Z_n \cos(n\Omega t + \phi_n) \tag{5}$$

$$\dot{z}(t) = \sum_{n=1}^{\infty} n\Omega[-a_n \sin(n\Omega t) + b_n \cos(n\Omega t)] = -\sum_{n=1}^{\infty} (n\Omega)Z_n \sin(n\Omega t + \phi_n) \tag{6}$$

$$\ddot{z}(t) = \sum_{n=1}^{\infty} -(n\Omega)^2[a_n \cos(n\Omega t) + b_n \sin(n\Omega t)] = -\sum_{n=1}^{\infty} (n\Omega)^2 Z_n \cos(n\Omega t + \phi_n) \tag{7}$$

which is an exact representation with infinitely many terms. Note that the relative displacement given by Eq. (5) accounts for the constant term a_0 resulting from the asymmetric system behavior. In order to obtain an approximate solution, Eqs. (5)–(7) have to be truncated to include finite number of terms (harmonics). The truncated form of Eq. (5) is

$$z_N(t) = a_0 + \sum_{n=1}^{N} [a_n \cos(n\Omega t) + b_n \sin(n\Omega t)] = a_0 + \sum_{n=1}^{N} Z_n \cos(n\Omega t + \phi_n) \tag{8}$$

which includes N harmonics. As the system has both quadratic and cubic stiffness nonlinearities, which are associated with the generation of predominant second and third harmonics in the response under hard forcing [23], the truncated Fourier series representation should contain sufficient terms ($N = 3$ is used in this work).

As mentioned in Section 3.3, the observed nonlinear damping was characterized as quadratic and attributed to air damping [65]. While numerical simulation easily handles the non-smooth absolute value function present in the physical model, it is required for the multi-term harmonic balance analysis to introduce an equivalent viscous damping coefficient c and re-express the equation of motion as

$$m\ddot{z} + c\dot{z} + k_1 z + k_2 z^2 + k_3 z^3 + m\ddot{y} = 0 \tag{9}$$

where the viscous damping coefficient is obtained by calculating the energy dissipated in the system by considering only the dominant harmonic as an approximation:

$$c = 2\zeta m\omega_n \left(1 + \gamma \frac{8\Omega^2 Z_1}{3\pi} \right) \tag{10}$$

Then, substitution of the truncated Fourier series into the equation of motion yields the residual function:

$$R(t) = m\ddot{z}_N + c\dot{z}_N + k_1 z_N + k_2 z_N^2 + k_3 z_N^3 + mA \cos(\Omega t) \tag{11}$$

Using the Galerkin method of mean weighted residuals, a system of algebraic equations in the harmonic amplitudes is generated:

$$\int_0^{2\pi/\Omega} R(t)dt = 0 \tag{12}$$

$$\int_0^{2\pi/\Omega} R(t)\cos(n\Omega t)dt = 0 \tag{13}$$

$$\int_0^{2\pi/\Omega} R(t)\sin(n\Omega t)dt = 0 \tag{14}$$

The choice to include a constant term (a_0) and three harmonics ($a_n, b_n; n = 1, 2, 3$) in the assumed solution yields a root finding problem of 7 equations for 7 unknowns:

$$
\begin{aligned}
& 8k_3 a_0^2 - 6k_3 b_1^2 a_2 + 6k_3 a_1^2 a_2 + 12k_3 a_0 b_3^2 + 12k_3 a_0 a_2^2 + 12k_3 a_0 b_2^2 + 12k_3 a_0 a_3^2 \\
& + 12k_3 a_0 a_1^2 + 12k_3 a_0 b_1^2 + 8k_1 a_0 + 4k_2 b_2^2 + 4k_2 a_3^2 + 4k_2 b_3^2 + 4k_2 a_1^2 + 4k_2 b_1^2 \\
& + 4k_2 a_2^2 + 8k_2 a_0^2 + 12k_3 b_1 a_2 b_3 + 12k_3 a_1 b_2 b_3 + 12k_3 a_1 a_2 a_3 + 12k_3 a_1 b_1 b_2 - 12k_3 b_1 b_2 a_3 = 0
\end{aligned}
\tag{15}
$$

$$
\begin{aligned}
& 4k_1 a_1 + 4mA + 3k_3 a_1^3 + 3k_3 a_1 b_1^2 + 6k_3 a_1 b_3^2 + 6k_3 a_1 b_2^2 + 6k_3 a_1 a_3^2 + 6k_3 a_1 a_2^2 + 12k_3 a_0 b_1 b_2 \\
& + 12k_3 a_0 a_2 a_3 + 12k_3 a_0 b_2 b_3 + 6k_3 a_1 b_1 b_3 + 3k_3 a_1^2 a_3 + 4k_2 a_1 a_2 - 3k_3 b_2^2 a_3 + 3k_3 a_2^2 a_3 - 3k_3 b_1^2 a_3 \\
& + 4k_2 b_2 b_3 + 4k_2 a_2 a_3 + 4k_2 b_1 b_2 + 4cb_1\Omega + 8k_2 a_0 a_1 + 12k_3 a_0^2 a_1 + 12k a_0 a_1 a_2 + 6k_3 a_2 b_2 b_3
\end{aligned}
$$

$$-4ma_1\Omega^2 = 0 \tag{16}$$

$$
\begin{aligned}
&12k_3a_0a_1b_2 - 12k_3a_0b_2a_3 + 12k_3a_0a_2b_3 - 12k_3a_0b_1a_2 + 6k_3a_2b_2a_3 - 6k_3a_1b_1a_3 + 6k_3b_1b_2^2 \\
&-3k_3a_2^2b_3 + 3k_3a_1^2b_1 + 12k_3a_0^2b_1 + 4k_2a_2b_3 - 4k_2b_2a_3 + 4k_2a_1b_2 - 4k_2b_1a_2 + 8k_2a_0b_1 + 3k_3a_1^2b_3 \\
&+6k_3b_1a_2^2 - 3k_3b_1^2b_3 + 6k_3b_1a_3^2 + 6k_3b_1b_3^2 - 4m\Omega^2b_1 - 4c\Omega a_1 + 3k_3b_1^3 + 4k_1b_1 = 0
\end{aligned}
\tag{17}
$$

$$
\begin{aligned}
&4k_1a_2 + 3k_3a_2^3 + 2k_2a_1^2 - 2k_2b_1^2 + 4k_2b_1b_3 + 3k_3a_2b_2^2 + 6k_3b_1^2a_2 + 6k_3a_1^2a_2 + 6k_3a_0a_1^2 \\
&-6k_3a_0b_1^2 + 8cb_2\Omega + 8k_2a_0a_2 + 4k_2a_0a_2 + 4k_2a_1a_3 - 16ma_2\Omega^2 + 12k_3a_0^2a_2 + 6k_3a_2b_3^2 \\
&+6k_3a_2a_3^2 + 6k_3a_1a_2a_3 + 6k_3b_1b_2a_3 - 6k_3b_1a_2b_3 + 6k_3a_1b_2b_3 + 12k_3a_0b_1b_3 + 12k_3a_0a_1a_3 = 0
\end{aligned}
\tag{18}
$$

$$
\begin{aligned}
&4k_1b_2 - 16m\Omega^2b_2 - 8c\Omega a_2 + 3k_3b_2^3 + 4k_2a_1b_3 + 4k_2a_1b_1 - 4k_2b_1a_3 + 3k_3a_2^2b_2 \\
&+6k_3b_2b_3^2 + 6k_3b_1^2b_2 + 6k_3b_2a_3^2 + 6k_3a_1^2b_2 + 12k_3a_0^2b_2 + 8k_2a_0b_2 + 12k_3a_0a_1b_1 \\
&-6k_3a_1b_2a_3 + 6k_3a_1a_2b_3 + 6k_3b_1a_2a_3 + 6k_3b_1b_2b_3 + 12k_3a_0a_1b_3 - 12k_3a_0b_1a_3 = 0
\end{aligned}
\tag{19}
$$

$$
\begin{aligned}
&12k_3a_0a_1a_2 - 12k_3a_0b_1b_2 + 6k_3b_1a_2b_2 + k_3a_1^3 + 4k_1a_3 + 3k_3a_3^3 - 36ma_3\Omega^2 \\
&+12k_3a_0^2a_3 + 3k_3a_3b_3^2 + 12cb_3\Omega - 3k_3a_1b_1^2 - 3k_3a_1b_2^2 + 3k_3a_1a_2^2 + 6k_3a_1^2a_3 \\
&+4k_2a_1a_2 + 6k_3b_2^2a_3 + 6k_3a_2^2a_3 + 6k_3b_1^2a_3 - 4k_2b_1b_2 + 8k_2a_0a_3 = 0
\end{aligned}
\tag{20}
$$

$$
\begin{aligned}
&3k_3b_3^3 + 4k_1b_3 - k_3b_1^3 + 6k_3a_1a_2b_2 - 12c\Omega - 36m\Omega^2b_3 + 3k_3b_1b_2^2 \\
&+6k_3a_2^2b_3 + 6k_3b_2^2b_3 + 3k_3a_1^2b_1 + 4k_2a_1b_2 + 4k_2b_1a_2 + 6k_3a_1^2b_3 - 3k_3b_1a_2^2 \\
&+6k_3b_1^2b_3 + 8k_2a_0b_3 + 3k_3a_3^2b_3 + 12k_3a_0^2b_3 + 12k_3a_0a_1b_2 + 12k_3a_0b_1a_2 = 0
\end{aligned}
\tag{21}
$$

Since a closed-form solution is impossible, the multivariate Newton–Raphson method is employed to solve for the unknowns. The problem is cast into vector form, with $\overrightarrow{x}_i$ being the ith iterate of the vector of a_0, a_n, and b_n:

$$\overrightarrow{f}(\overrightarrow{x}) = \overrightarrow{0} \tag{22}$$

$$\overrightarrow{x}_{i+1} = \overrightarrow{x}_i - [J(\overrightarrow{x}_i)]^{-1}\overrightarrow{f}(\overrightarrow{x}_i) \tag{23}$$

It should be highlighted once again that the main reason for keeping higher harmonics ($n=2$, 3) is to explore the effect of these terms in the frequency response with comparisons to experimental measurements and numerical simulations. Otherwise including more than one harmonic term drastically complicates the resulting system of algebraic equations. Nevertheless this procedure of accounting for higher harmonics in the harmonic balance analysis is more efficient than time-domain numerical simulations. For systems with low damping, time-domain numerical simulations must involve large numbers of cycles to converge to steady-state response, whereas only a few iterations of the Newton–Raphson method yield convergent harmonic balance. Depending on the choice of simulation parameters, time-domain simulations may take an order of magnitude or more time than the multi-term harmonic balance method solved with the Newton–Raphson method.

4.2. Single-harmonic closed-form solution

If the constant term (a_0) is neglected and only a single harmonic term is used in Eq. (8), the resulting algebraic equation is simplified dramatically and it is possible to obtain a closed-form frequency response equation. Eqs. (12)–(14) reduce to

$$\int_0^{2\pi/\Omega} R(t)\cos(\Omega t + \phi)dt = 0 \tag{24}$$

$$\int_0^{2\pi/\Omega} R(t)\sin(\Omega t + \phi)dt = 0 \tag{25}$$

and the assumed response form to be used in the residual expression is

$$z(t) = Z_1\cos(\Omega t + \phi) \tag{26}$$

yielding

$$k_1Z_1 - mZ_1\Omega^2 + \tfrac{3}{4}k_3Z_1^3 + mA\cos\phi = 0 \tag{27}$$

$$-cZ_1\Omega + mA\sin\phi = 0 \tag{28}$$

The phase term in Eqs. (27) and (28) can then be eliminated to give the frequency response equation:

$$\left(k_1Z_1 - mZ_1\Omega^2 + \tfrac{3}{4}k_3Z_1^3\right)^2 + (cZ_1\Omega)^2 = (mA)^2 \tag{29}$$

which is the same result that can be obtained using alternative perturbation methods [23,66] for this simplified case of using a single harmonic. It should be noted that the quadratic nonlinearity term vanishes in this single-term approximation. Therefore the error in single-term approximation is expected to grow with increasing contribution from the quadratic stiffness term.

5. Experimental results, model validation, and case study

Using the experimental setup shown in Fig. 4, up and down frequency sweep experiments are conducted at fixed base acceleration levels to extract the nonlinear frequency response functions of the M-shaped harvester for verification of broadband behavior and validation of the mathematical model and its solution. Effects of higher harmonics in harmonic balance analysis is discussed and also demonstrated in a case study for electromagnetic energy harvesting.

5.1. Model validation at different excitation levels

By using the feedback shaker system (Fig. 4), up and down frequency sweep experiments are conducted at rms (root-mean-square) base acceleration levels of 0.03g, 0.05g, and 0.07g. The results of these experiments are shown in Fig. 8. The displacement frequency response curves discussed in this section are relative to the inertial frame, i.e. the displacement x (see Fig. 5) is plotted in the frequency response graphs.

In Fig. 8, the bottom, middle, and top rms displacement response relationships correspond to low base acceleration rms values of 0.03g, 0.05g, and 0.07g, respectively. The system exhibits significant nonlinear behavior in all three cases. As the base acceleration level increases, the increase in peak displacement amplitude becomes saturated, while the bandwidth of the response continues to grow. The system shows 3 dB (half-power point) bandwidths of 1.0 Hz, 1.7 Hz, and 2.7 Hz for the respective excitation levels. As a fraction of the linear resonant frequency, the bandwidths are 7.5, 12.7, and 20.1 percent, respectively. To compare, an ideal linear system with the same linear parameters would have a 3 dB bandwidth of approximately 0.03 Hz (with a much higher maximum amplitude due to the very light linear damping). Consequently the M-shaped harvester offers 3200, 5600, and 8900 percent bandwidth enhancement at the rms base excitation levels of 0.03g, 0.05g, and 0.07g, respectively. The nonlinear system displays substantial bandwidth enhancement even for these low base acceleration levels.

In order to validate the mathematical model presented in this work, both time-domain numerical simulations (using ode45 in MATLAB) and harmonic balance (Section 4) results are obtained and compared with experiments. For the lowest base excitation level of 0.03g rms, experimental, numerical, and harmonic balance results are shown in Fig. 9 along with a detail view of the large response branch. The harmonic balance results are given for 1-term and 3-term solutions. It is observed that the agreement between the harmonic balance and time-domain numerical simulations is improved substantially as the number of harmonics is increased from $N=1$ to $N=3$. Specifically the 1-term harmonic balance solution underestimates the response amplitude over the large-amplitude branch and overestimates the frequency of the upper saddle-node bifurcation point. Overall, the 3-term solution exhibits much better agreement with the experimental results and time-domain numerical solution as compared to the 1-term solution.

Further comparisons are given for the excitation levels of 0.05g and 0.07g rms. For all excitation levels, the 3-term harmonic balance solution agrees closely with the time-domain numerical simulation. In the neighborhood of the up-sweep jump in the frequency response, both deviate from the experimental result. The numerical results overestimate the response, likely due to additional unmodeled dissipation and stiffness effects. Damping is assumed to be well-modeled by a combination of linear viscous and quadratic damping in the lumped-parameter model, while other dissipative effects may be significant. Terms of higher order may also start to be significant in the elastic restoring force. In all cases, the time-domain simulation and 3-term harmonic balance solution provide a better estimate of the frequency at which the bifurcation in the upper branch occurs as compared to the 1-term harmonic balance solution (Figs. 10 and 11).
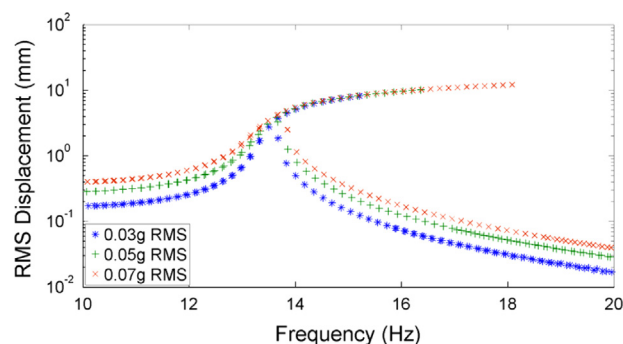

Fig. 8. Experimental displacement frequency response curves of the M-shaped oscillator at 0.03g, 0.05g, and 0.07g rms base acceleration levels (up- and down-sweep curves are shown together).
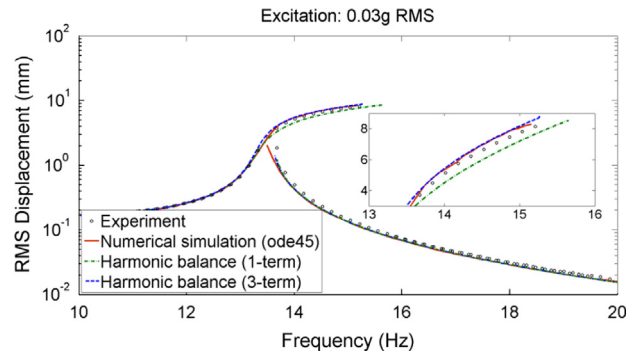
Fig. 9. Displacement frequency response curves of the M-shaped oscillator at 0.03*g* rms base acceleration level for up and down sweep: experimental measurement, time-domain numerical simulation, and harmonic balance solutions (1-term and 3-term).
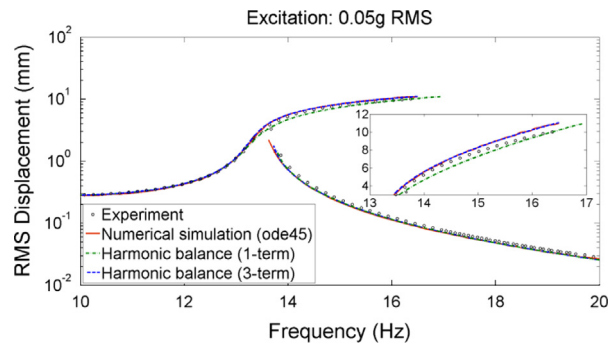

Fig. 10. Displacement frequency response curves of the M-shaped oscillator at 0.05*g* rms base acceleration level for up and down sweep: experimental measurement, time-domain numerical simulation, and harmonic balance solutions (1-term and 3-term).

Fig. 11. Displacement frequency response curves of the M-shaped oscillator at 0.07*g* rms base acceleration level for up and down sweep: experimental measurement, time-domain numerical simulation, and harmonic balance solutions (1-term and 3-term).
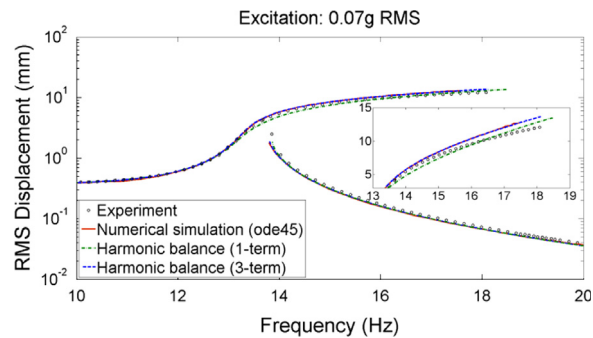
Overall, the experimental and simulated data are observed to be in very close agreement. The 0.03*g* and 0.05*g* cases show agreement at all frequencies, while the 0.07*g* case shows a discrepancy between the magnitude and frequency of the top of the upper branch. The simulation predicts a maximum rms amplitude of 12.8 mm at a frequency of 17.5 Hz. The experimental values are 12.1 mm at 18.1 Hz. Increasing the value of γ would reduce the error of the maximum amplitude, but would increase the error of the maximum amplitude frequency. The value of $\gamma = 1$ s/m is deemed acceptable for this model for all excitation levels covered in this work.

Experimental evidence of high bandwidth behavior at remarkably low excitation amplitudes is of particular interest. Studies involving the nonlinear vibrations of magnetoelastic oscillators showed only very slight nonlinear behavior at excitation levels around 0.1*g* and required levels of 0.3–0.5*g* to display pronounced nonlinear behavior [30,34–36,38]. The M-shaped oscillator presented here suggests substantial reduction in the required excitation level from magnetoelastic oscillators by an order of magnitude. Additionally, the configuration presented in this work exhibits the desired broadband behavior due to a simpler arrangement of components without any magnetoelastic restoring force.

5.2. On the effect of static component and higher harmonics

Further details regarding the effect of higher harmonics are discussed next, focusing on different kinematic forms of the response. Electromechanical coupling is more closely related to velocity than displacement in basic energy harvesting techniques [1,2] (e.g. piezoelectric transduction and electromagnetic induction). Fig. 12 displays the contributions of the different harmonics to the displacement, velocity, and acceleration responses at the 0.07g rms base acceleration level. For the M-shaped oscillator explored in this work, the nonlinearities are related to either displacement or velocity according to Eq. (1); and as shown in Fig. 12, the first harmonic dominates all other components of the displacement and velocity responses by at least an order of magnitude. The small magnitude of the DC component of the displacement as well as the higher harmonics does not, however, mean that they can be ignored in harmonic balance analysis. These different harmonics are coupled in Eqs. (15)–(21), and ignoring seemingly insignificant higher harmonics in the response can lead to considerable errors in the prediction of important characteristics of the system, such as the frequency and magnitude of the response at the saddle-node bifurcation point in the upper branch.

Additionally, since the structure is intended for vibrational energy harvesting, the inclusion of higher harmonics may be even more important. Compared with the relative contribution of the different harmonics to displacement, the contribution of each successive harmonic to the velocity increases linearly with harmonic number. For energy harvesting systems, velocity is the variable that couples the electrical and mechanical domains, e.g. due to linear piezoelectricity and Faraday's law of induction, making higher harmonics very significant, as demonstrated next.
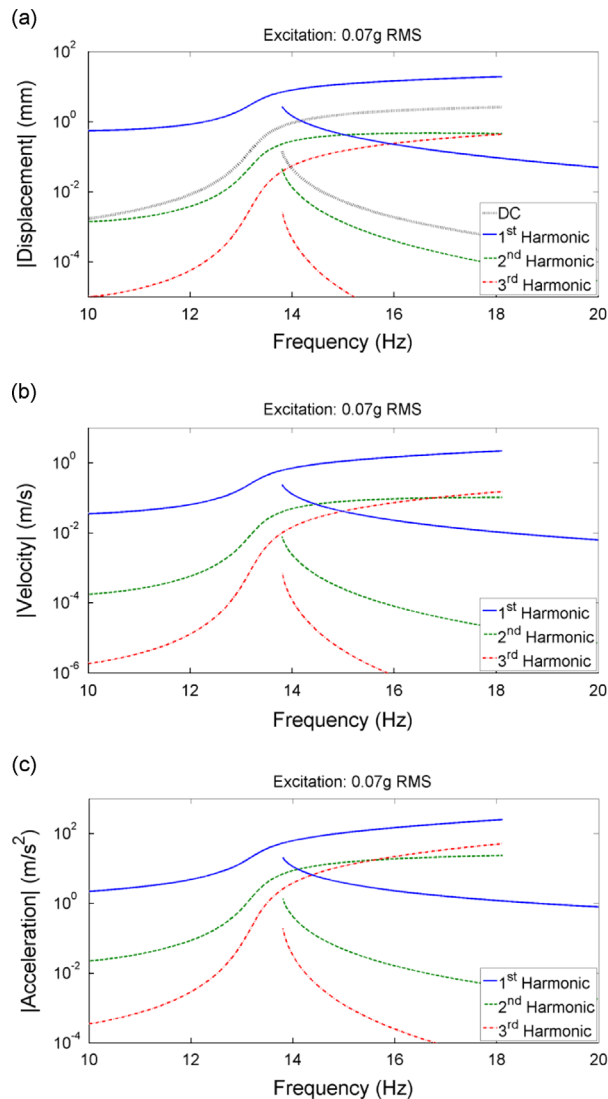

Fig. 12. Magnitudes of the harmonic balance terms versus frequency for different kinematic forms of the response: (a) displacement; (b) velocity; and (c) acceleration.

5.3. Case study for electromagnetic energy harvesting

In order to demonstrate the potential of the M-shaped configuration for broadband electrical power generation, and to illustrate the effects of higher harmonics in the power output, consider an electromagnetic energy harvesting implementation for the case of negligible coil inductance and linear electromechanical coupling as in Mann and Sims [26]. We further assume zero internal (coil) resistance for simplicity. The governing electromechanical equations are then

$$m\ddot{z} + 2\zeta m\omega_n \dot{z}(1 + \gamma|\dot{z}|) + k_1 z + k_2 z^2 + k_3 z^3 - \theta i = -m'\ddot{y} \tag{30}$$

$$R_l i + \theta \dot{z} = 0 \tag{31}$$

where $i(t)$ is the electric current, θ is the electromechanical coupling, and R_l is the electrical load resistance. Eqs. (30) and (31) can then be combined to give

$$m\ddot{z} + (c_m + c_e)\dot{z} + k_1 z + k_2 z^2 + k_3 z^3 = -m'\ddot{y} \tag{32}$$

Here, c_m is the mechanical viscous damping coefficient including the equivalent quadratic damping according to Eq. (10), $c_m = 2\zeta m\omega_n(1 + 8\Omega^2\gamma Z_1/3\pi)$, while c_e is the electrical damping coefficient, $c_e = \theta^2/R_l$. The average electrical power output is calculated using

$$P_{ave} = i_{rms}^2 R_l = \left(\frac{\theta \dot{z}_{rms}}{R_l}\right)^2 R_l = c_e \dot{z}_{rms}^2 \tag{33}$$

which can be analyzed for a range of c_e values by using multi-term and single-term harmonic balance expressions for the vibration response given by Eqs. (8) and (26), respectively. The only modification required in the harmonic balance analysis of Section 4 is to update the damping coefficient given by Eq. (10) to account for the electrical damping:

$$c = c_m + c_e = 2\zeta m\omega_n\left(1 + \gamma\frac{8\Omega^2 Z_1}{3\pi}\right) + \frac{\theta^2}{R_l} \tag{34}$$

For instance, the single-term solution for the average electrical power is

$$P_{ave} = \tfrac{1}{2} c_e \Omega^2 Z_1^2 \tag{35}$$

where Z_1 is obtained from

$$\left(k_1 Z_1 - m Z_1 \Omega^2 + \tfrac{3}{4} k_3 Z_1^3\right)^2 + (c_m + c_e)^2 (Z_1 \Omega)^2 = (mA)^2 \tag{36}$$

For a set of electrical damping coefficient values in the range of $0 < c_e/c_m < 2$, average power output frequency response curves are plotted based on the 3-term harmonic balance solution in Fig. 13a for 0.07g rms base excitation. The two-dimensional view of the average power frequency response curves in Fig. 13b reveals that the maximum power output corresponds to the case of $c_e = c_m$ as in linear electromagnetic energy harvesters (with linear electromechanical coupling) in the absence of internal load resistance [67]. More importantly, Fig. 13b clearly shows that the frequency bandwidth of large amplitude response shrinks monotonically with increased electrical damping. Wide bandwidths correspond to low values of electrical damping ($0 < c_e/c_m \ll 1$); however, low values of c_e/c_m are associated with low power output as the fundamental trade-off. The maximum power output is obtained for $c_e = c_m$ with reduced bandwidth as compared to the cases of $0 < c_e/c_m < 1$. Further increase in the electrical damping to the range of $c_e/c_m > 1$ results in both reduced power output and reduced frequency bandwidth, gradually eliminating the advantages of the nonlinear M-shaped design over is linear counterpart.

Finally, the comparison of 1-term and 3-term solutions of the power frequency response curves for the case of $c_e = c_m$ is given in Fig. 14. Recall from the previous graphs (Section 5.1) that the 3-term solution agrees very well with the time-domain numerical solution. As can be seen from this figure, in agreement with the discussion given in Section 5.2, the harvested power can be very sensitive to higher harmonics of the M-shaped oscillator. The upper saddle-node bifurcation point is predicted by the 1-term harmonic balance solution as 15.42 Hz, overestimating the 3-term solution of 15.04 Hz. Therefore the electrical power predictions of the 1-term harmonic balance solution between these two frequencies would be off by several orders of magnitude (since only the lower branch exists in the more accurate 3-term solution between 15.04 Hz and 15.42 Hz). The large-amplitude branch of the 3-term harmonic balance solution lies in the frequency range of 13.78 Hz to 15.04 Hz. In this frequency range, the 1-term solution underestimates the power output by more than 20 percent. For instance, the errors in the 1-term solution relative to 3-term solution at the frequencies of 14 Hz, 14.5 Hz, and 15 Hz are 29, 25, and 21 percent, respectively. Clearly the M-shaped energy harvester requires multi-term harmonic balance analysis for the accurate representation of its dynamics and prediction of the harvested power output.

6. Conclusions

An M-shaped bent beam with clamped end conditions is investigated theoretically and experimentally for bandwidth enhancement in vibration energy harvesting from base excitation. The proposed M-shaped oscillator made of spring steel is
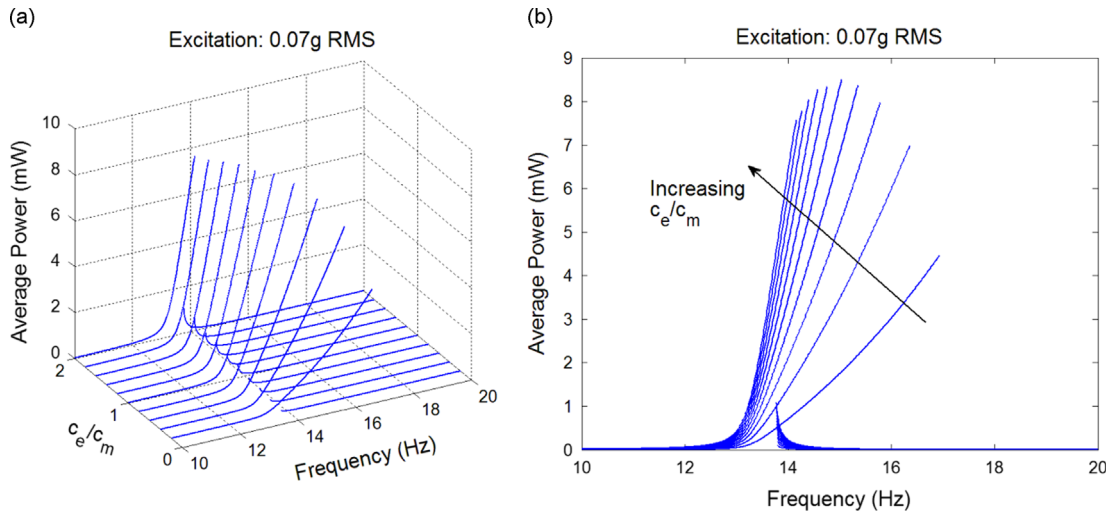
Fig. 13. Average electrical power output frequency response curves for different values of the normalized electrical damping coefficient c_e/c_m: (a) 3-D view of power output versus frequency and normalized electrical damping and (b) 2-D view to visualize the maximum power case that corresponds to $c_e=c_m$ and the monotonic shortening of the frequency bandwidth of large-amplitude branch with increased electrical damping (0.07g rms base acceleration).
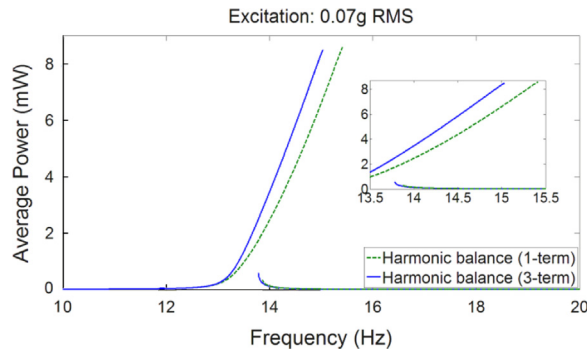

Fig. 14. Comparison of average electrical power output frequency response curves obtained from the 1-term and 3-term harmonic balance solutions for $c_e=c_m$ (0.07g rms base acceleration).

simpler to fabricate as it does not require extra discrete components to assemble. Furthermore the asymmetric nonlinear behavior of this configuration can easily be pronounced to yield broadband behavior under low excitation levels. Linear and nonlinear system parameters extracted from experiments are used to develop a lumped-parameter mathematical model. A quadratic damping term is included in the model and observed to be sufficient in order to account for nonlinear dissipative effects. In the absence of such a nonlinear dissipative term, the model tends to overestimate the frequency and amplitude of the upper saddle-node bifurcation point. A multi-term harmonic balance solution is developed to study the effects of higher harmonics and a constant term. Additionally, a single-term closed-form frequency response equation is also extracted and compared with the multi-term harmonic balance solution. Specifically, it is observed that the single-term solution overestimates the frequency of upper saddle-node bifurcation point and underestimates the response amplitude in the large response branch. Multi-term harmonic balance solutions can be as accurate as time-domain solutions, and offer the advantage of substantially reduced computation time. Overall, very good agreement is observed between the model predictions and experimental measurements of the nonlinear frequency response under different base excitation levels. Substantial bandwidth enhancement with increasing base excitation is validated experimentally, analytically, and numerically. As compared to the 3 dB bandwidth of the corresponding linear system (with the same damping linear ratio), the M-shaped oscillator offers 3200, 5600, and 8900 percent bandwidth enhancement at the root-mean-square base excitation levels of 0.03g, 0.05g, and 0.07g, respectively. A case study is also given for electromagnetic energy harvesting, revealing the importance of higher harmonics and the need for multi-term harmonic balance analysis for predicting the power output accurately. Due to the existence of multiple regions of large strain and kinetic energy, the M-shaped oscillator can be conveniently employed in piezoelectric and electromagnetic energy harvesting as well as hybrid combinations thereof.

Acknowledgment

References

[1] A. Erturk, D.J. Inman, *Piezoelectric Energy Harvesting*, Wiley, Chichester, UK, 2011.
[2] N. Elvin, A. Erturk, *Advances in Energy Harvesting Methods*, Springer, New York, USA, 2013.
[3] P. Glynne-Jones, M.J. Tudor, S.P. Beeby, N.M. White, An electromagnetic, vibration-powered generator for intelligent sensor systems, *Sensors and Actuators A—Physical* 110 (1–3) (2004) 344–349.
[4] D.P. Arnold, Review of microscale magnetic power generation, *IEEE Transactions on Magnetics* 43 (11) (2007) 3940–3951.
[5] N.G. Elvin, A.A. Elvin, An experimentally validated electromagnetic energy harvester, *Journal of Sound and Vibration* 330 (10) (2011) 2314–2324.
[6] S. Roundy, P.K. Wright, J. Rabaey, A study of low level vibrations as a power source for wireless sensor nodes, *Computer Communications* 26 (11) (2003) 1131–1144.
[7] P.D. Mitcheson, P. Miao, B.H. Stark, E.M. Yeatman, A.S. Holmes, T.C. Green, MEMS electrostatic micropower generator for low frequency operation, *Sensors and Actuators A—Physical* 115 (2–3) (2004) 523–529.
[8] C.P. Le, E. Halvorsen, O. Søråsen, E.M. Yeatman, Microscale electrostatic energy harvester using internal impacts, *Journal of Intelligent Material Systems and Structures* 23 (13) (2012) 1409–1421.
[9] S. Roundy, P.K. Wright, A piezoelectric vibration based generator for wireless electronics, *Smart Materials & Structures* 13 (5) (2004) 1131–1142.
[10] A. Erturk, D.J. Inman, An experimentally validated bimorph cantilever model for piezoelectric energy harvesting from base excitations, *Smart Materials & Structures* 18 (2009) 2.
[11] C. De Marqui Junior, A. Erturk, D.J. Inman, An electromechanical finite element model for piezoelectric energy harvester plates, *Journal of Sound and Vibration* 327 (1) (2009) 9–25.
[12] L. Wang, F.G. Yuan, Vibration energy harvesting by magnetostrictive material, *Smart Materials and Structures* 17 (4) (2008). (Article ID 045009).
[13] A. Adly, D. Davino, A. Giustiniani, C. Visone, Experimental tests of a magnetostrictive energy harvesting device toward its modeling, *Journal of Applied Physics* 107 (9) (2010). (Article ID 09A935).
[14] R.D. Kornbluh, R. Pelrine, H. Prahlad, A. Wong-Foy, B. McCoy, S. Kim, J. Eckerle, T. Low. From boots to buoys: promises and challenges of dielectric elastomer energy harvesting, *Proceedings of SPIE Smart Structures and Materials+Nondestructive Evaluation and Health Monitoring*, International Society for Optics and Photonics, 2011.
[15] M. Aureli, C. Prince, M. Porfiri, S.D. Peterson, Energy harvesting from base excitation of ionic polymer metal composites in fluid environments, *Smart materials and Structures* 19 (1) (2010) 015003.
[16] H.A. Sodano, D.J. Inman, G. Park, A review of power harvesting from vibration using piezoelectric materials, *Shock and Vibration Digest* 36 (3) (2004) 197–206.
[17] S.R. Anton, H.A. Sodano, A review of power harvesting using piezoelectric materials (2003–2006), *Smart Materials and Structures* 16 (3) (2007) R1.
[18] S. Priya, Advances in energy harvesting using low profile piezoelectric transducers, *Journal of Electroceramics* 19 (1) (2007) 167–184.
[19] K.A. Cook-Chennault, N. Thambi, A.M. Sastry, Powering MEMS portable devices—a review of non-regenerative and regenerative power supply systems with special emphasis on piezoelectric energy harvesting systems, *Smart Materials and Structures* 17 (4) (2008) 043001.
[20] J.M. Renno, M.F. Daqaq, D.J. Inman, On the optimal energy harvesting from a vibration source, *Journal of Sound and Vibration* 320 (1–2) (2009) 386–405.
[21] N.G. Elvin, A.A. Elvin, A general equivalent circuit model for piezoelectric generators, *Journal of Intelligent Material Systems and Structures* 20 (1) (2009) 3–9.
[22] M. Daqaq, R. Masana, A. Erturk, D. Quinn, On the role of nonlinearities in vibration energy harvesting: a critical review and discussion, *ASME Applied Mechanics Reviews* 66 (2014). (in press), http://dx.doi.org/10.1115/1.4026278.
[23] A.H. Nayfeh, D.T. Mook, *Nonlinear Oscillations*, Wiley-VCH Verlag GmbH, Weinheim, Germany, 2008.
[24] J. Guckenheimer, P. Holmes. Nonlinear oscillations, dynamical systems, and bifurcations of vector fields. Vol. 42. Springer Verlag, New York, USA, 1983.
[25] S.G. Burrow, L.R. Clare, A. Carrella, D. Barton. Vibration energy harvesters with non-linear compliance, *Proceedings of SPIE*, 2008.
[26] B.P. Mann, N.D. Sims, Energy harvesting from the nonlinear oscillations of magnetic levitation, *Journal of Sound and Vibration* 319 (1–2) (2009) 515–530.
[27] R. Ramlan, M.J. Brennan, B.R. Mace, I. Kovacic, Potential benefits of a non-linear stiffness in an energy harvesting device, *Nonlinear Dynamics* 59 (4) (2010) 545–558.
[28] M.F. Daqaq, Response of uni-modal duffing-type harvesters to random forced excitations, *Journal of Sound and Vibration* 329 (18) (2010) 3621–3631.
[29] P. Green, K. Worden, K. Atallah, N. Sims, The benefits of Duffing-type nonlinearities and electrical optimisation of a mono-stable energy harvester under white Gaussian excitations, *Journal of Sound and Vibration* 331 (20) (2012) 4504–4517.
[30] S.C. Stanton, C.C. McGehee, B.P. Mann, Reversible hysteresis for broadband magnetopiezoelastic energy harvesting, *Applied Physics Letters* 95 (17) (2009) 174103–174103-3.
[31] F. Cottone, H. Vocca, L. Gammaitoni, Nonlinear energy harvesting, *Phys Rev Lett* 102 (8) (2009) 080601.
[32] L. Gammaitoni, I. Neri, H. Vocca, Nonlinear oscillators for vibration energy harvesting, *Applied Physics Letters* 94 (2009) 16.
[33] C.R. McInnes, D.G. Gorman, M.P. Cartmell, Enhanced vibrational energy harvesting using nonlinear stochastic resonance, *Journal of Sound and Vibration* 318 (4–5) (2008) 655–662.
[34] S.C. Stanton, C.C. McGehee, B.P. Mann, Nonlinear dynamics for broadband energy harvesting: investigation of a bistable piezoelectric inertial generator, *Physica D—Nonlinear Phenomena* 239 (10) (2010) 640–653.
[35] S.C. Stanton, B.A. Owens, B.P. Mann, Harmonic balance analysis of the bistable piezoelectric inertial generator, *Journal of Sound and Vibration* 331 (15) (2012) 3617–3627.
[36] A. Erturk, J. Hoffmann, D.J. Inman, A piezomagnetoelastic structure for broadband vibration energy harvesting, *Applied Physics Letters* 94 (2009) 25.
[37] F. Moon, P.J. Holmes, A magnetoelastic strange attractor, *Journal of Sound and Vibration* 65 (2) (1979) 275–296.
[38] A. Erturk, D.J. Inman, Broadband piezoelectric power generation on high-energy orbits of the bistable Duffing oscillator with electromechanical coupling, *Journal of Sound and Vibration* 330 (10) (2011) 2339–2353.
[39] G. Litak, M.I. Friswell, C.A.K. Kwuimy, S. Adhikari, M. Borowiec, Energy harvesting by two magnetopiezoelastic oscillators with mistuning, *Theoretical and Applied Mechanics Letters* 2 (4) (2012) 043009–043009-5.
[40] A. Sneller, P. Cette, B. Mann, Experimental investigation of a post-buckled piezoelectric beam with an attached central mass used to harvest energy, *Proceedings of the Institution of Mechanical Engineers, Part I: Journal of Systems and Control Engineering* 225 (4) (2011) 497–509.
[41] R. Masana, M.F. Daqaq, Relative performance of a vibratory energy harvester in mono-and bi-stable potentials, *Journal of Sound and Vibration* 330 (24) (2011) 6036–6052.
[42] A. Arrieta, P. Hagedorn, A. Erturk, D. Inman, A piezoelectric bistable plate for nonlinear broadband energy harvesting, *Applied Physics Letters* 97 (10) (2010) 104102–104102-3.
[43] B. Mann, B. Owens, Investigations of a nonlinear energy harvester with a bistable potential well, *Journal of Sound and Vibration* 329 (9) (2010) 1215–1226.

[44] S.D. Nguyen, E. Halvorsen, I. Paprotny, Bistable springs for wideband microelectromechanical energy harvesters, *Applied Physics Letters* 102 (2) (2013) 023904–023904-4.

[45] M.F. Daqaq, Transduction of a bistable inductive generator driven by white and exponentially correlated Gaussian noise, *Journal of Sound and Vibration* 330 (11) (2011) 2554–2564.

[46] S. Ali, S. Adhikari, M. Friswell, S. Narayanan, The analysis of piezomagnetoelastic energy harvesters under broadband random excitations, *Journal of Applied Physics* 109 (7) (2011) 074904.

[47] P. Kumar, S. Narayanan, S. Adhikari, M. Friswell, Fokker–Planck equation analysis of randomly excited nonlinear energy harvester, *Journal of Sound and Vibration* 333 (7) (2014) 2040–2053.

[48] G. Litak, M. Friswell, S. Adhikari, Magnetopiezoelastic energy harvesting driven by random excitations, *Applied Physics Letters* 96 (21) (2010) 214103–214103-3.

[49] G. Litak, M. Borowiec, M.I. Friswell, S. Adhikari, Energy harvesting in a magnetopiezoelastic system driven by random excitations with uniform and Gaussian distributions, *Journal of Theoretical and Applied Mechanics* 49 (3) (2011) 757–764.

[50] S. Zhao, A. Erturk, On the stochastic excitation of monostable and bistable electroelastic power generators: relative advantages and tradeoffs in a physical system, *Applied Physics Letters* 102 (10) (2013) 103902–103902-5.

[51] M. Ghandchi Tehrani, S.J. Elliott, Extending the dynamic range of an energy harvester using nonlinear damping, *Journal of Sound and Vibration* 333 (3) (2014) 623–629.

[52] L. Tang, Y. Yang, C.K. Soh, Toward broadband vibration-based energy harvesting, *Journal of Intelligent Material Systems and Structures* 21 (18) (2010) 1867–1897.

[53] S.P. Pellegrini, N. Tolou, M. Schenk, J.L. Herder, Bistable vibration energy harvesters: a review, *Journal of Intelligent Material Systems and Structures* 24 (2013) 1303–1312.

[54] J. Twiefel, H. Westermann, Survey on broadband techniques for vibration energy harvesting, *Journal of Intelligent Material Systems and Structures* 24 (2013) 1291–1302.

[55] R. Harne, K. Wang, A review of the recent research on vibration energy harvesting via bistable systems, *Smart Materials and Structures* 22 (2) (2013) 023001.

[56] D.S. Nguyen, E. Halvorsen, G.U. Jensen, A. Vogl, Fabrication and characterization of a wideband MEMS energy harvester utilizing nonlinear springs, *Journal of Micromechanics and Microengineering* 20 (2010) 12.

[57] L.G.W. Tvedt, D.S. Nguyen, E. Halvorsen, Nonlinear behavior of an electrostatic energy harvester under wide- and narrowband excitation, *Journal of Microelectromechanical Systems* 19 (2) (2010) 305–316.

[58] L.N. Virgin, *Vibration of Axially Loaded Structures*, Vol. 393, Cambridge University Press, Cambridge, 2007.

[59] G.K. Ottman, H.F. Hofmann, A.C. Bhatt, G.A. Lesieutre, Adaptive piezoelectric energy harvesting circuit for wireless remote power supply, *IEEE Transactions on Power Electronics* 17 (5) (2002) 669–676.

[60] Y. Shu, I. Lien, Analysis of power output for piezoelectric energy harvesting systems, *Smart Materials and Structures* 15 (6) (2006) 1499.

[61] N. Kong, D.S. Ha, A. Erturk, D.J. Inman, Resistive impedance matching circuit for piezoelectric energy harvesting, *Journal of Intelligent Material Systems and Structures* 21 (13) (2010) 1293–1302.

[62] S.G. Burrow, P.D. Mitcheson, B.H. Stark, *Power Conditioning Techniques for Energy Harvesting, in Advances in Energy Harvesting Methods*, Springer, New York, USA, 2013, 323–343.

[63] W.T. Thomson, *Theory of Vibration with Applications*, Taylor & Francis, UK, 1993.

[64] L. Meirovitch, *Fundamentals of Vibrations*, McGraw Hill, New York, 2001.

[65] J. Bandstra, Comparison of equivalent viscous damping and nonlinear damping in discrete and continuous vibrating systems, *Journal of Vibration, Acoustics Stress and Reliability in Design* 105 (3) (1983) 382–392.

[66] A.H. Nayfeh, *Perturbation Methods*, Wiley-VCH Verlag GmbH, Weinheim, Germany, 2008.

[67] N. Stephen, On energy harvesting from ambient vibration, *Journal of Sound and Vibration* 293 (1) (2006) 409–425.